CONF-9003128--3
UCRL- JC-103302
PREPRINT

MODELING PULSE DRIVEN ANTENNA SYSTEMS WITH FINITE DIFFERENCES

Marvin Barth
Steve Pennock
Richard Ziolkowski
Robert McLeod

This paper was prepared for submittal to
the 6th Annual Review of Progress in
Applied Computational Electromagnetics
Monterey, CA, 3/19-22/90

March 1990

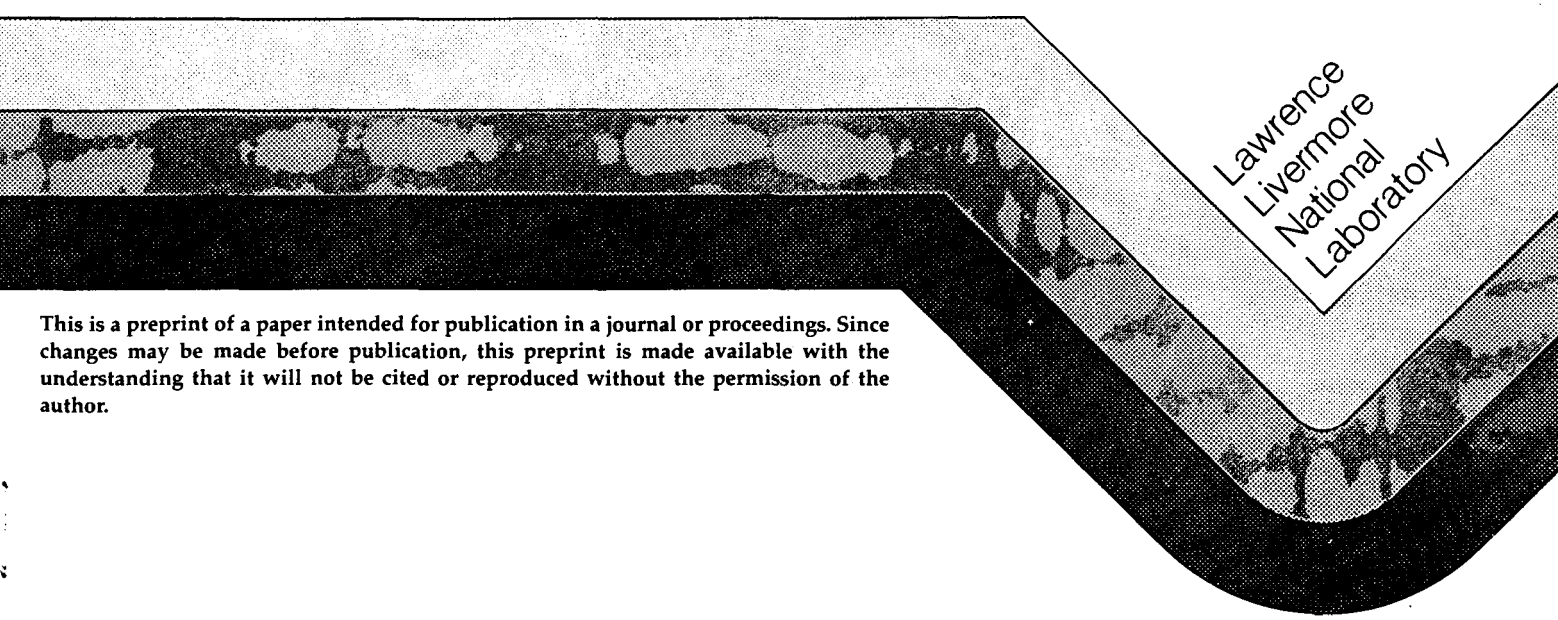

MODELING PULSE DRIVEN ANTENNA SYSTEMS WITH FINITE DIFFERENCES

Marvin Barth, Steve Pennock, Richard Ziolkowski,
and Robert McLeod
Lawrence Livermore National Laboratory
P. O. Box 5504, L-156
Livermore, CA 94550

UCRL-JC--103302

DE90 010682

ABSTRACT

We have developed a capability of modeling the performance of general, pulse driven, antenna systems. Our approach is to use TSAR, a three dimensional finite difference time domain (FDTD) code, to model the antenna structure and the surrounding near field environment. We then use a far field projection algorithm to obtain its far field response. Specifically, this algorithm utilizes the tangential electric and magnetic fields at a specified surface of the TSAR FDTD computational volume and calculates the resulting fields far from the equivalent magnetic and electric sources.

This approach will be illustrated by considering the TEB antenna system. The system is modeled with the code and the results are compared with anechoic chamber data.

INTRODUCTION

In analyzing the response of an antenna system to transit pulses, the capability of computer modeling the system provides several advantages. Besides cost, the ability is provided to calculate responses from different driving pulses and modifications to the drive system.

At Lawrence Livermore National Laboratory (LLNL) we have in the past developed a sophisticated three dimension FDTD code termed TSAR. A FDTD code time step calculates the fields at each point of a three dimensional grid and, because of computer memory size, is limited to near field phenomenon. A FDTD code also has three other limitations:

(1) There are reflections of the fields at the boundaries of the geometrical volume being modeled. These reflections are reduced by applying the Mur boundary conditions: but, at oblique angles to the boundary, are never eliminated.

(2) There are trade-offs between a smaller grid size for modeling accuracy and the desire to include as much of the geometry volume as possible.

(3) Because mechanical derivatives replace the partial derivatives in Maxwell's equations, there are diffusion and dispersion errors. These errors appear as high frequency noise and are proportional to the grid size.

Last year, we also developed the FAR code which projects near field values of the electric and magnetic field over an imaginary surface to the far field using the equivalence principle. Specifically, the near electric and magnetic fields are represented by point dipoles and the far field is computed by summing the far fields of the dipoles. The FAR code is limited in accuracy by the density of the point dipole sampling of the near electric and magnetic fields on the surface. The FAR code has been incorporated into TSAR and this option we will term the TSAR-FAR code. With the exception of now not being limited to the near field, the limitations of the TSAR-FAR code are those of the typical FDTD code plus one other. This other limitation is illustrated in Figure 1 where a two dimensional FDTD grid is shown with the problem boundary. (Mur boundary conditions are assumed.) The Electric Field Measuring Surface (i.e., the equivalent surface on which the electric and magnetic fields are sampled) is depicted a few cells in from the problem boundary. Because waves at oblique incidence reflect from the problem boundary, the number of time steps for the problem must be limited such that the reflected wave is not included in the sampled fields. Figure 1 shows that the Maximum Problem Run Time is the time for the antenna transmitted wave to reach problem boundary surface, be reflected, and return to the Electric Field Measuring Surface.

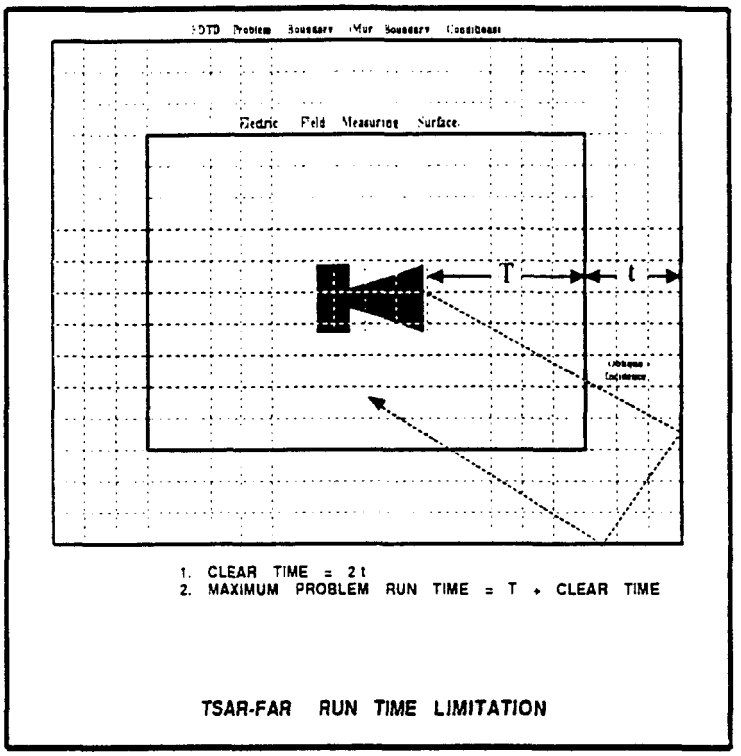

Figure 1
FDTD Representation Showing The Maximum Run Time Limitation

In this paper, our objective is to demonstrate the use of the TSAR-FAR code to model transit pulse antenna systems. We will do this by comparing the computed TSAR-FAR results with experimental anechoic chamber data taken from the TEB antenna system. The results of the comparison will be pattern plot errors and mean rms errors.

The two systems, computational and experimental, are shown in Figure 2. In the anechoic chamber, a UK0 pulse drives the TEB antenna system and a B-Dot probe is used to measure the far field. The 13 measurement points relative to the TEB antenna are shown in Table 1. At each of the 13 points in the vertical and horizontal planes, the received signal is stored as TEBxx files (where xx represent 01 to 13). There are two limitations for the experimental system:

(1) Even though it is an anechoic chamber, there were wall reflections in the data. In order to mitigate these reflections, we cut the received data in half to 512 points for each time record.

(2) The receiving system characteristics (other than the fact that a B-Dot probe was used) were unknown at the time of the data reduction. We developed a filter (termed the Cardinal Point filter and applied to the computational results) to compensate for this.

The driving UK0 pulse is shown in Figure 3(a) where the time interval is set to 1.0 and it is seen that the UK0 pulse is almost 1024 point long.

Referring again to Figure 2, we calculated the antenna response by modeling the TEB antenna and using the TSAR-FAR code. Because of the Maximum Problem Run Time limitation, we used a different driving pulse. This driving pulse, EXCIT0, is shown in Figure 3(b) where the time interval is 1.0. As can be seen, this pulse is only 26 time steps long. The frequency characteristics of both pulses are below 2.0 Mhz. The TSAR-FAR output time records were at the same positions as the TEB measuring points shown in Table 1 and are named TFxx(RAW) (where xx represent 01 to 13). For model detail, we used a grid size spacing of one inch. The time interval corresponding to this grid size is 4.23626e-11 seconds while the time interval for the anechoic chamber data is 1.953e-11 seconds. In Figure 2, the inputs and outputs inclosed with square boxes are the input data available for the remainder of this paper, i.e:

(1) the TSAR-FAR driver, EXCIT0,

(2) the 13 TSAR-FAR output files, TFxx(RAW),
(3) the anechoic chamber driver, UK0, and
(4) the 13 anechoic chamber measurements, TEBxx.

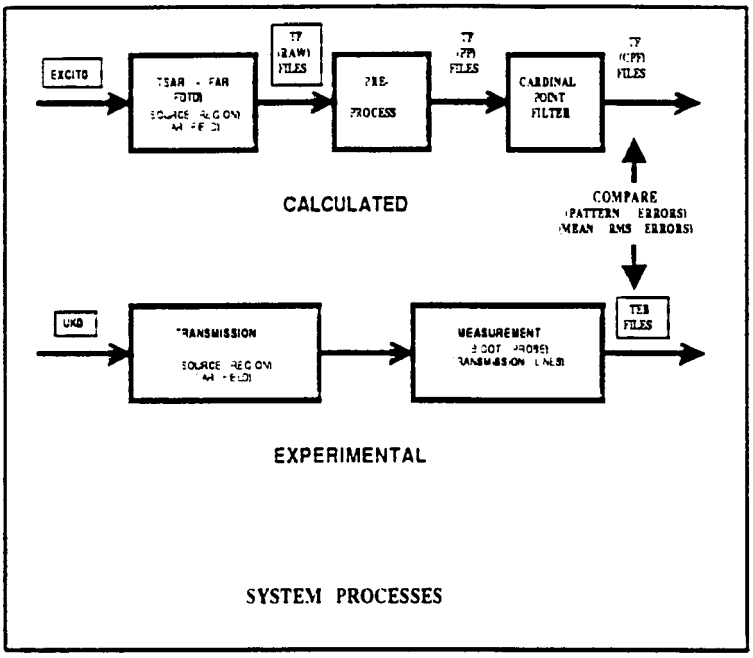

Figure 2
The Calculated & Experimental System Block Diagrams

TEB File	Polar Angle	Azimuth Angle
01	090	000
02	"	030
03	"	045
04	"	060
05	"	090
06	"	120
07	"	150
08	060	000
09	030	"
10	000	"
11	030	180
12	060	"
13	090	"

Table 1: Positions of Anechoic Chamber Measurements Relative To TEB

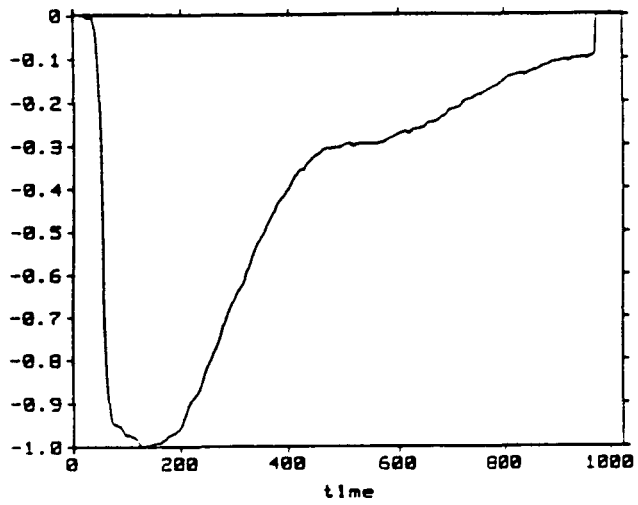

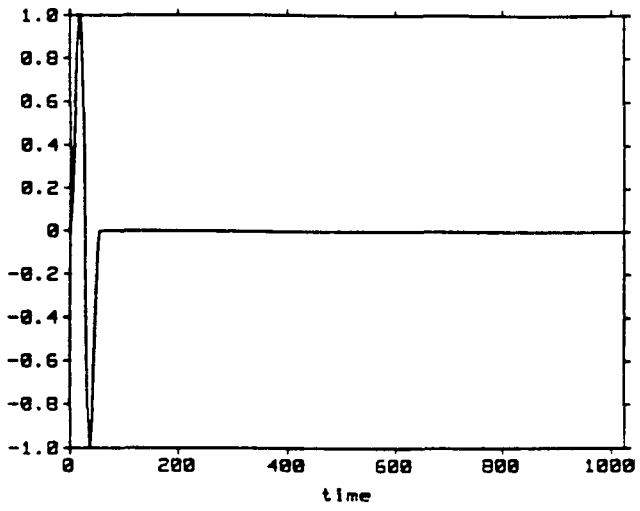

Figure 3(a) Figure 3(b)
Driving Pulses: (a) UK0 & (b) EXCIT0

DISCUSSION

Figures 4(a) and (b) show typical time records for the TF and TEB data. In Figure 4(b) the high frequency dispersion and diffusion noise is apparent.

As indicated in Figure 2, all of our processing was done to the TF data. We used a LLNL signal processing code termed SIG to accomplish the processing. The processing was accomplished in two major steps. the output of the first is the preprocessed TF(PP) files and the second output (after the Cardinal Point filter is applied) is the TF(CPF) files.

The first set of preprocessing from the TF(RAW) to the TF(PP) files was the following (all done with records of 1024 points):

(1) We resampled the TF(RAW) and EXCIT0 data so that all time records (both calculated and experimental) had time intervals of 1.953e-11 seconds. We also compared the original and resampled time records in both the time and frequency domains to check that aliasing did not occur.

(2) We aligned the TEB and TF time records so that the first peak of both records occured at the same time.

(3) To eleminate the high frequency diffusion and dispersion noise we used a low pass butterworth filter (order=8, zero phase) on the TF data.

(4) To convert the TF data so that it corresponded to the B-Dot probe data, we differentiated the TF data.

(5) We exchanged the driving function EXCIT0 for the UK0 pulse. Our method of accomplishing this was to:

(a) find the impulse response for the TF data with EXCIT0 as the driving function by using SIG to generate an ARMAX filter model. and

(b) find the convolution of the above impulse response with the UK0 pulse.

The resulting time records were then cut to 512 point to produce the TF(PP) files.

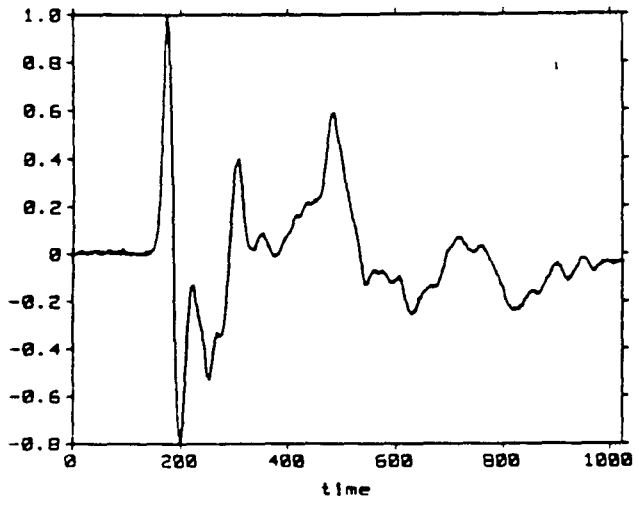

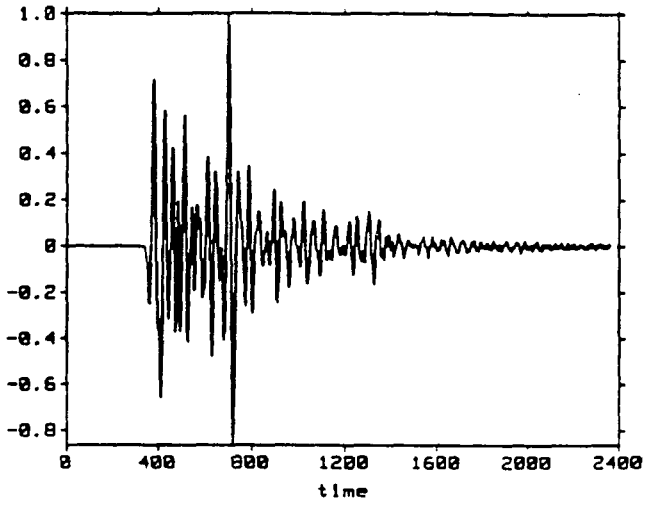

Figure 4(a) Figure 4(b)
Raw Data: (a) TEB04 & (b) TF(Raw)04

TF Impulse	Polar Angle	Azimuth Angle
01	090	000
05	090	090
05	090	090
10	000	000
10	000	080
13	090	000

Table 2: Positions For Construction Of Cardinal Point Filter

We next constructed a filter to account for the measurement receiving characteristics, wall and boundary reflections, and other miscellaneous noise. The filter is the average of the impulse responses between the TF(PP) and the TEB time records at the six cardinal spherical points shown in Table 2. Finally, we applied this Cardinal Point filter to the TF(PP) data to obtain the TF(CPF) data Figure 5 shows typical time records for the TF(CPF) and TEB data.

We made two types of comparisons between the TF(CPF) and TEB data:

(1) the vertical and horizontal energy pattern plots over a 360 degree range, and

(2) the mean rms point error for corresponding TF and TEB data.

Figures 6 and 7 show the energy plots for processed and filtered horizontal and vertical planes. Figures 8 and 9 show the corresponding energy plot error rates. The horizontal plots show the boundary and wall reflections were excessive at 60 and 90 degrees. Other than these points, there is good agreement.

Figure 10 shows the mean rms point errors for the 13 comparison points. The average of the mear rms errors is 4.948 %

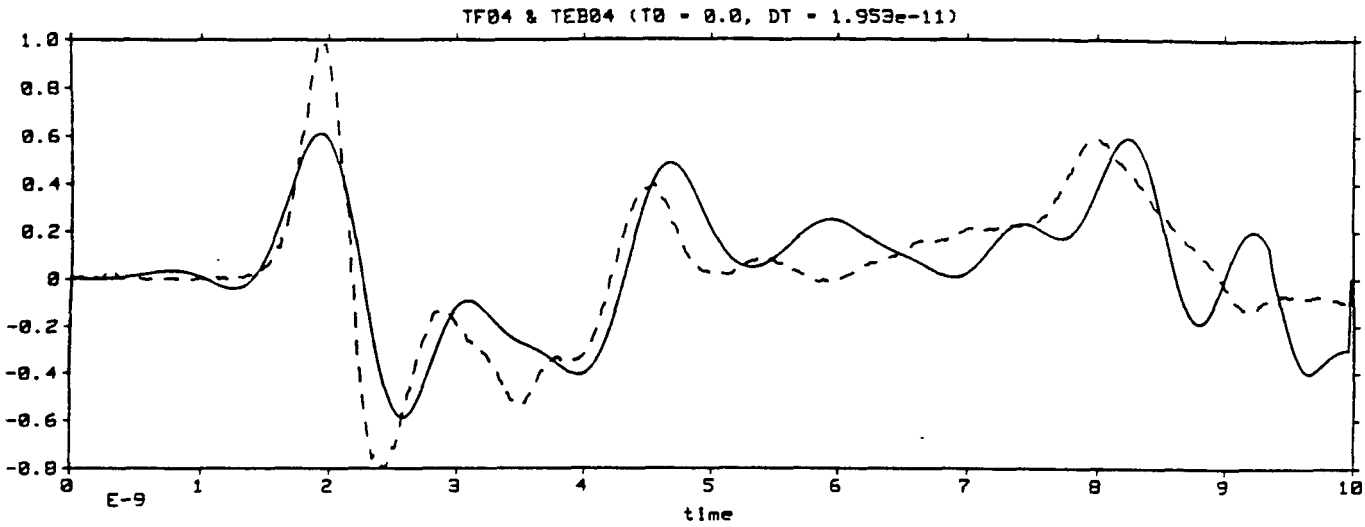

Figure 5
Comparison between TEB & Processed Filtered TF Data
(TF(CPF)04 & TEB04)

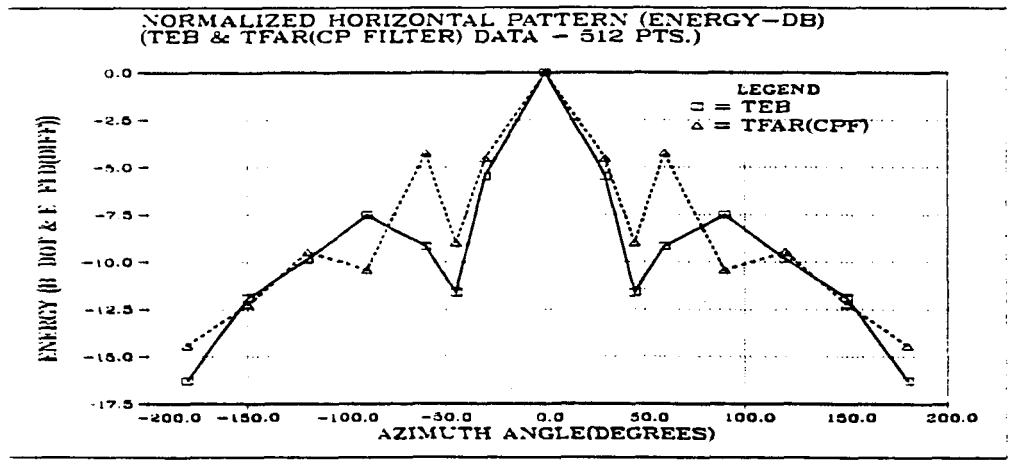

Figure 6
Normalized Horizontal Energy Plot

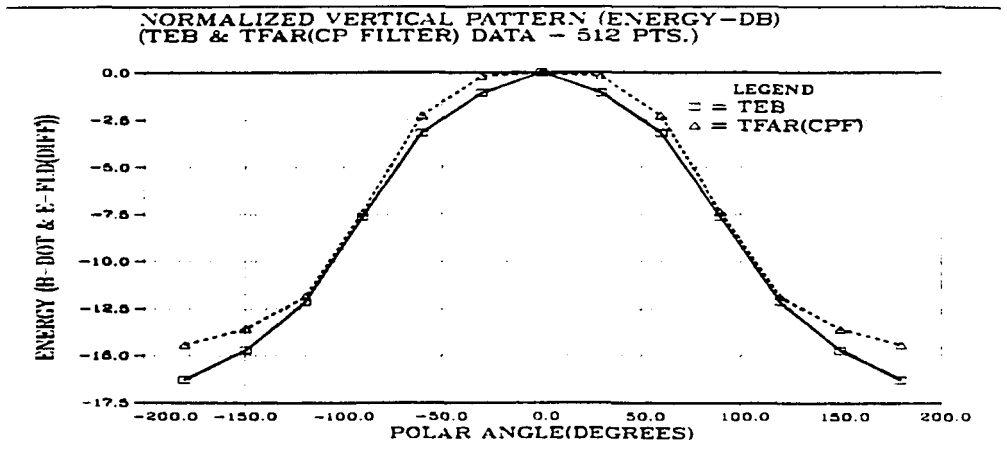

Figure 7
Normalized Vertical Energy Plot

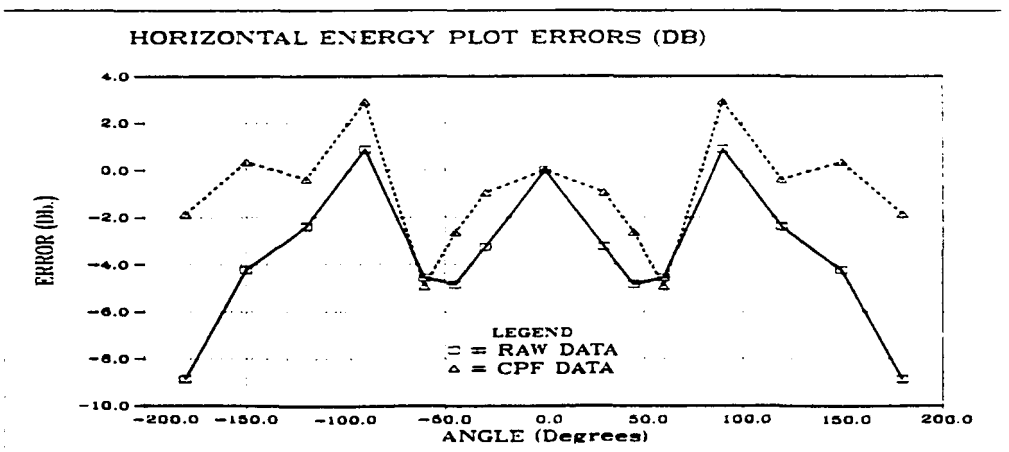

Figure 8
Horizontal Energy Plot Errors

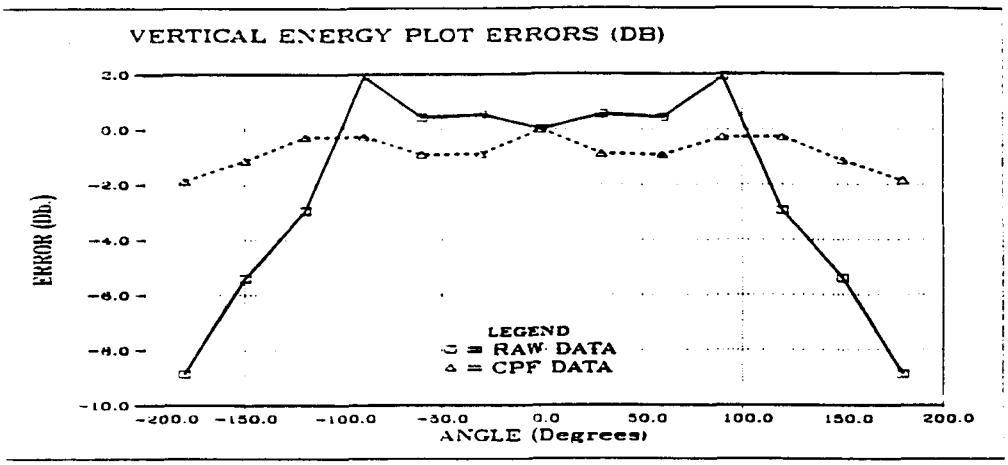

Figure 9
Vertical Energy Plot Errors

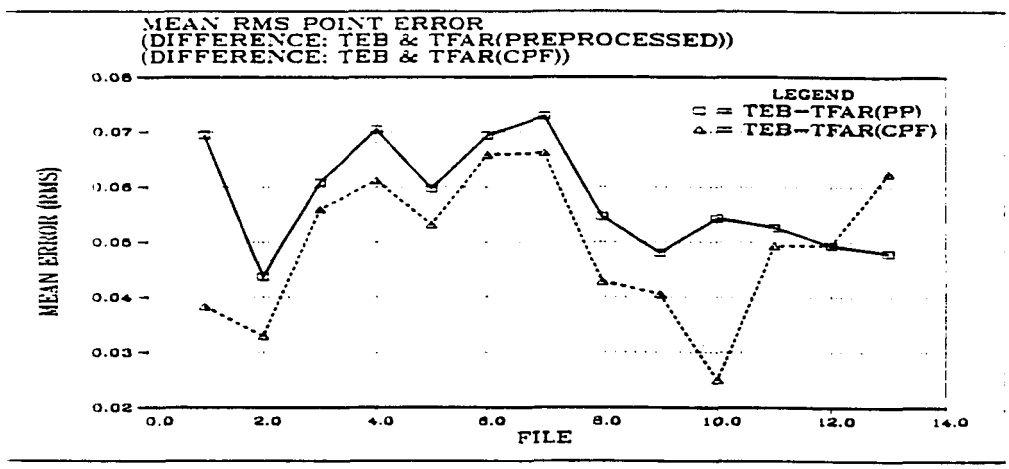

Figure 10
Mean RMS Point Error

CONCLUSIONS

FDTD codes have the limitation of modeling only the near fields. With the option of the TSAR-FAR code, the far field can be modeled provided the Maximum Problem Run Time is not exceeded. For a given computer memory, and therefore a fixed problem FDTD grid, this equates to limiting the model size and detail.

Work performed under the auspices of the U.S. Department of Energy by Lawrence Livermore National Laboratory under Contract W-7405-Eng-48.